Fuel 142 (2015) 152–163

Contents lists available at ScienceDirect

Fuel

journal homepage: www.elsevier.com/locate/fuel

Large-eddy simulation of pulverized coal jet flame – Effect of oxygen concentration on NO_x formation

Masaya Muto [a,*], Hiroaki Watanabe [b], Ryoichi Kurose [a], Satoru Komori [a], Saravanan Balusamy [c], Simone Hochgreb [c]

[a] Department of Mechanical Engineering and Science, Kyoto University, Kyoto daigaku-Katsura, Nishikyo-ku, Kyoto 615-8540, Japan
[b] Energy Engineering Research Laboratory, Central Research Institute of Electric Power Industry, 2-6-1 Nagasaka, Yokosuka 240-0196, Japan
[c] Department of Engineering, University of Cambridge, Trumpington Street, Cambridge CB2 1PZ, United Kingdom

HIGHLIGHTS

- Large-eddy simulation is applied to a pulverized coal flame with oxy-firing conditions.
- Effect of oxygen concentration on NO_x formation are investigated.
- Peak value of the formed NO increases with increasing the O_2 concentration.
- When equivalence ratio is larger than unity, NO decreases after its peak value.

ARTICLE INFO

Article history:
Received 13 July 2014
Received in revised form 20 October 2014
Accepted 22 October 2014
Available online 13 November 2014

Keywords:
Pulverized coal combustion
Oxy-fuel combustion
NO formation
Swirl jet flame
Large-eddy simulation

ABSTRACT

Large-eddy simulation is applied to a laboratory-scale open-type pulverized coal flame generated by a triple stream burner, and the NO production and reduction in oxy-fuel condition are investigated for the first time. Pulverized Cerrejon coal which is classified as bituminous coal is used as a fuel. The results show that regardless of the equivalence ratio, as the O_2 concentration increases from 21% to 40%, O_2 consumption becomes marked because gas temperature rises and oxidation reaction is enhanced by the higher concentration of O_2. Also, NO is formed rapidly due to the oxidation reaction of nitrogen from volatile matter of coal, and its concentration reaches a few hundred ppm further downstream. After the rapid formation, in the case of equivalence ratio larger than unity, NO decreases, because the reducing atmosphere becomes dominant due to the lack of O_2. The trend becomes significant as the O_2 concentration in the carrier gas increases from 21% to 40%. In the case of equivalence ratio less than unity, on the other hand, NO does not decrease clearly, because the oxidizing atmosphere contributes to the further formation of NO. Present study shows the usefulness of the large-eddy simulations for predicting the characteristics of pulverized coal flames.

© 2014 Elsevier Ltd. All rights reserved.

1. Introduction

Coal is still an important energy resource to satisfy the large demand for low cost electricity in Asian countries, as coal reserves are much more abundant than those of other fossil fuels and widely distributed all over the world. However, the emission intensities of carbon dioxide (CO_2), nitrogen oxide (NO_x) and sulfur oxide (SO_x) by using coal are generally larger than those by using other fossil fuels [1]. It is therefore important to develop clean coal technology for pulverized coal fired power plants, in order to control such emissions and to reduce the environmental impact. Regarding the reduction of environmental impact of CO_2, carbon capture and sequestration (CCS) is expected as a key technology, and it is believed that oxy-fuel pulverized coal combustion, in which gas mixture of oxygen (O_2) and CO_2 are used instead of air as oxidizer, has advantages for CCS, with low cost by means of only a retrofit of existing pulverized coal fired power plants [2].

Previous experimental and numerical investigations on oxy-fuel coal combustion technology have been reviewed in several papers [3–6]. In most of those papers, although the flow and gas temperature are measured at selected points in the combustion chamber, the concentration of pollutants is measured only at the outlet of the combustion chamber. Therefore, it is still difficult to clarify the formation mechanism of NO_x and SO_x inside the chamber. In parallel, recent simulations using computational fluid dynamics

* Corresponding author. Tel.: +81 75 383 3737; fax: +81 75 383 3613.
E-mail address: muto@me.kyoto-u.ac.jp (M. Muto).

http://dx.doi.org/10.1016/j.fuel.2014.10.069
0016-2361/© 2014 Elsevier Ltd. All rights reserved.

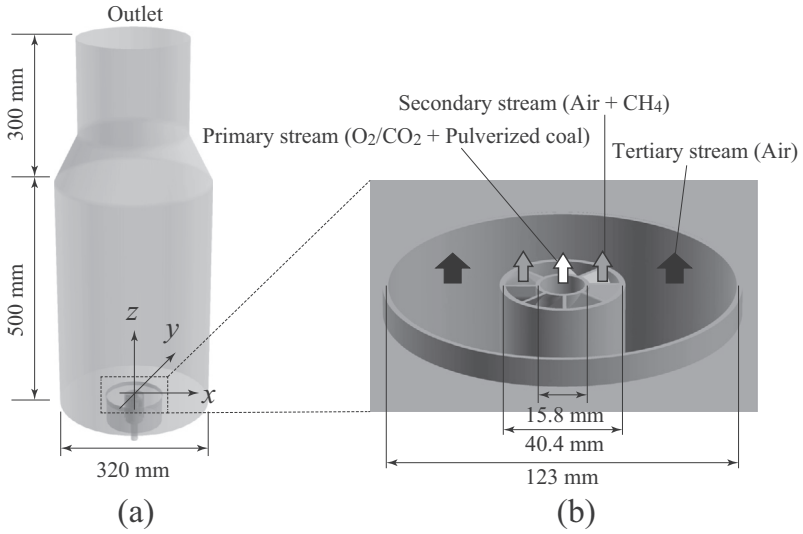

Fig. 1. Schematic diagrams of (a) computational domain and (b) burner configuration.

Table 1
Injection conditions of gas mixture and coal in primary stream.

Case	Carrier gas (O_2/CO_2) (%)	Coal feeding rate (g/s)	Equivalence ratio
1	21/76	0.31	1.73
2	30/67	0.45	
3	40/57	0.60	
4	21/76	0.10	0.69
5	30/67	0.15	
6	40/57	0.20	

Table 2
Coal properties [43].

Type of coal	Cerrejon
Density	640 kg/m^3
Proximate analysis	(wt%)
Moisture	5.8
Volatile matter	34.8
Fixed carbon	50.8
Ash	8.6
Ultimate analysis	(wt%)
Carbon	69.2
Hydrogen	4.4
Oxygen	9.98
Nitrogen	1.42
Combustible sulfur	0.58

such as Reynolds-averaged Navier–Stokes (RANS) simulation (e.g. [7–15]) and large-eddy simulation (LES, e.g. [10,16–24]) have been applied to oxy-fuel coal combustion [25–29] and revealing certain advantages of LES compared to RANS simulation in prediction of local distributions of chemical species concentrations and gas temperature [30]. However, there have been no predictions of NO_x formation for oxy-fuel pulverized coal flame by means of LES.

The purpose of this study is therefore to investigate the effects of O_2 concentration and equivalence ratio on the NO_x formation process in oxy-fuel pulverized coal flame generated using a laboratory-scale triple stream burner by means of LES, for various operating conditions of O_2 concentration in the carrier gas.

2. Numerical simulation

The LES solver used here is the FrontFlow/red developed by CRIEPI (Central Research Institute of Electric Power Industry), Kyoto University, and NuFD (Numerical Flow Designing CO., Ltd.).

2.1. Mathematical models and numerical method

The pulverized coal particles are tracked in Lagrangean manner using the equation of motion for dispersed particles. Coal devolatilization was simulated by a first-order single reaction model in which devolatilization rate is given as Arrhenius equation. In this study, parameters in Arrhenius equation for each coal were obtained by pyrolysis simulation using a FLASHCHAIN model [31]. The chemical mechanism for volatile matter and CH_4 considered in this study consists of two-step global reactions [11], and the char burning rate was calculated using Field's model [32]. In this study, LES with a standard subgrid-scale model was adopted. Second-order central differences approximations were used to discretize the spatial derivative, while 5% of the first-order upwind scheme was blended with the central differences. The time marching was based on the fractional step method [33] in which the third-order Adams–Moulton scheme is used for velocity prediction. The time step for the calculation, Δt, is set to 10^{-5} s.

2.2. Chemical reactions for NO formation

In the present LES, only the production of NO was taken into account because the NO_x emitted to the atmosphere from combusting pulverized coal consists mostly of NO, with much lower concentrations of NO_2 and N_2O [5]. NO originating from nitrogen, N_2, in air (thermal NO and prompt NO) and that from N in coal (fuel NO) were considered. The thermal NO and the prompt NO were calculated by Zeldovich and Fenimore [34] mechanisms, respectively [35]. In the reactions of Zeldovich, Fenimore and reburn, which are described below, the kinetic parameters proposed by Bedat et al. [35] are employed. In the study by Bedat et al. reactions for the formation of NO are expressed in global reaction forms as $N_2 + O_2 \rightarrow 2NO$, $N_2 + VM + O_2 \rightarrow 2NO + VM$, and $2NO + VM \rightarrow N_2 + O_2 + VM$, where VM is volatile matter. Fuel NO originating from volatile N was assumed to be formed through instantaneous evolution in the form of hydrogen cyanide (HCN) [36], and the minor evolution of

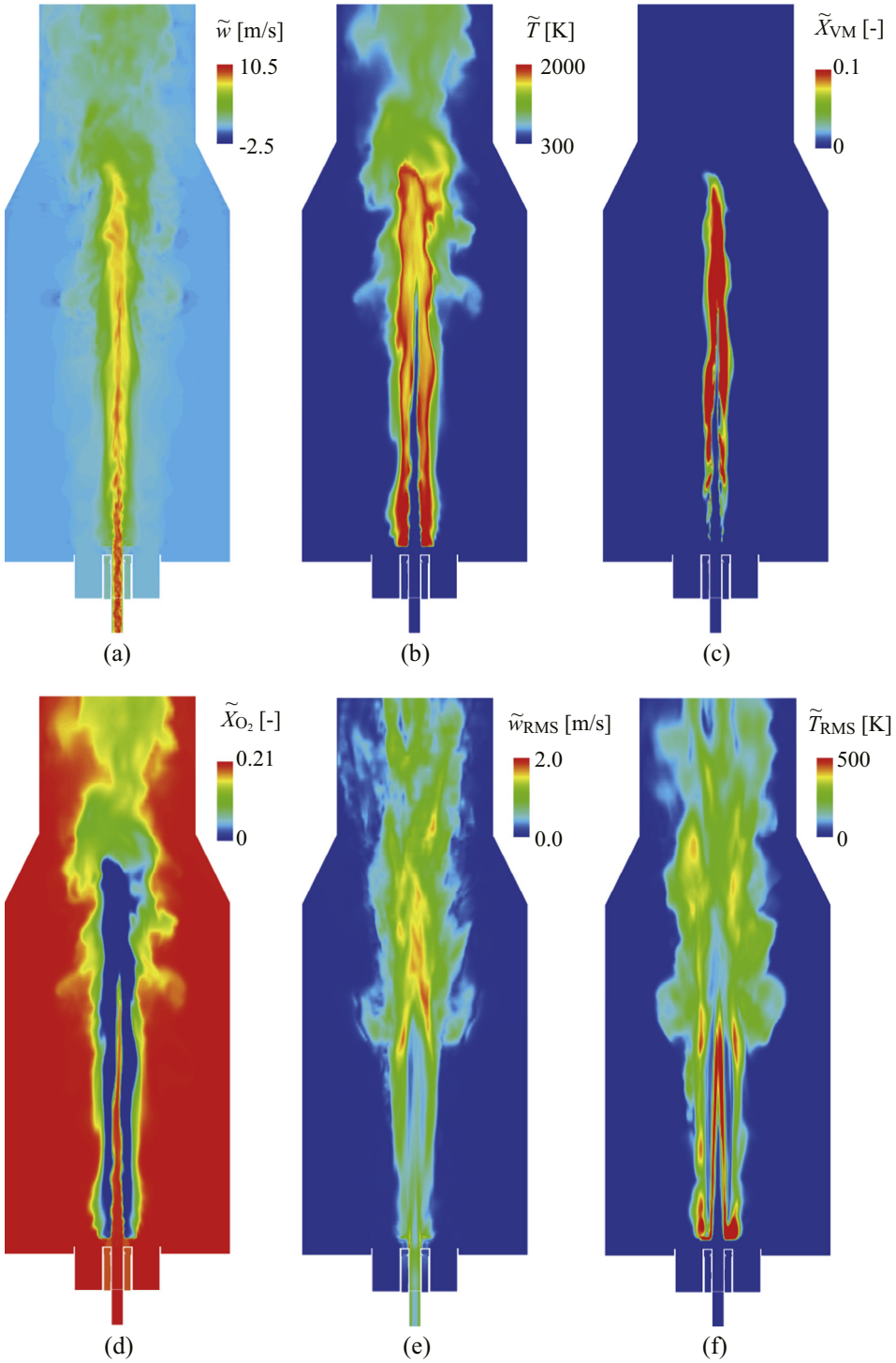

Fig. 2. Instantaneous distributions of (a) axial velocity $\bar{w}$, (b) gas temperature $\bar{T}$, and mole fractions of (c) volatile matter $\bar{X}_{VM}$, (d) O_2, $\bar{X}_{O_2}$, and RMS values of (e) axial velocity $\bar{w}_{RMS}$ and (f) gas temperature $\bar{T}_{RMS}$ on the x–z plane at $y = 0$ mm for Case 1.

ammonia (NH_3) was neglected. Formation of char NO was also calculated using DeSoete's models [37,38]. The rate of NO reduction by char is also considered using Levy's model [39] which takes account of the external surface area of char and NO partial pressure in the gas mixture. The Scale Similarity Filtered Reaction Rate Model (SSFRRM) [40] was used as the subgrid scale (SGS) model for the NO reactions as well as for the combustion reactions of the volatile matter and CH_4. The SSFRRM attempts to model the effect of SGS fluctuations on the filtered reaction rate by assuming that the largest of the sub grid scales are dynamically similar to the smallest of the resolved scales [41]. Although some of these NO formation and reduction mechanisms involve global reaction rates, the NO formation and reduction models have been validated by comparing with the experiments and confirmed to be able to capture the general feature even in the LES targeting a large test furnace in our previous papers [10,17].

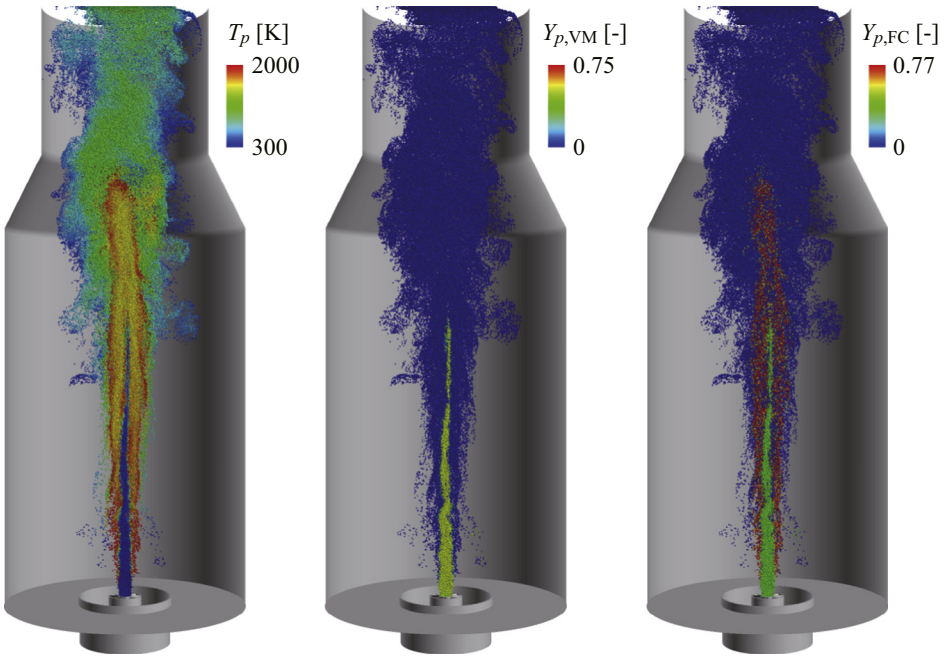

Fig. 3. Instantaneous distributions of (a) particle temperature T_p, and mass fractions of (b) volatile matter $Y_{p,VM}$ and (c) fixed carbon $Y_{p,FC}$ in coal particles behind the x–z plane at $y = 0$ mm for Case 1.

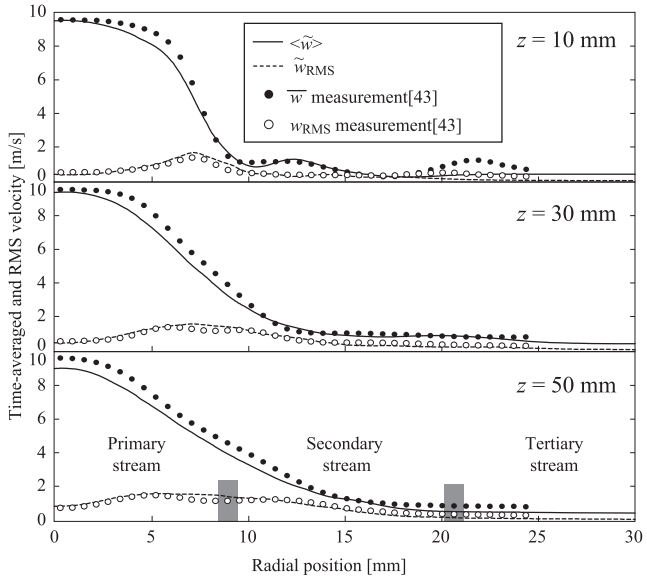

Fig. 4a. Comparisons of radial distributions of time-averaged and RMS velocities in axial direction at three downstream locations between measurement and LES for non-reacting flows. (See above-mentioned references for further information.)

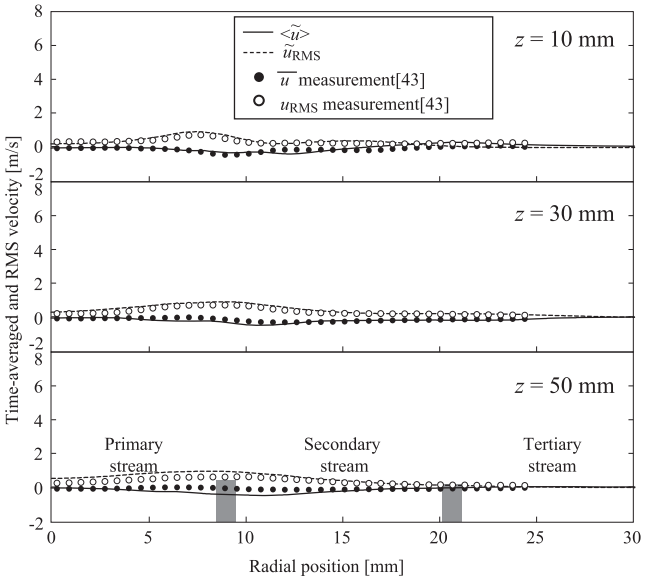

Fig. 4b. Comparisons of radial distributions of time-averaged and RMS velocities in radial direction at three downstream locations between measurement and LES for non-reacting flows. (See above-mentioned references for further information.)

2.3. Computational domain and conditions

The configuration of the computational domain and the laboratory-scale triple stream burner [42,43] are shown in Fig. 1. The burner consists of three coaxial pipes and an axial swirler. The axial swirler has eight evenly-spaced vanes of 1 mm thickness at an angle of 45 degree to the burner exit plane. The swirl number calculated from its geometry is 0.77. In the primary stream, pulverized coal particles are carried by the gas mixture of O_2 and CO_2 at an axial velocity of 7.32 m/s and a temperature of 300 K. The concentrations of the gas mixture and coal for the primary stream are listed in Table 1. For the velocity profile of the primary stream, turbulent fully developed flow in a smooth pipe was adopted. To promote coal ignition, methane (CH_4) is also issued in the primary stream at the rate of 3% of total volume. In the experiment [43], there is an additional 6% of N_2 in the oxidizing mixture due to the ingress of ambient air in the coal carrying process, but the present LES focuses on the NO formation derived only from coal particles so that the additional N_2 is neglected. To ignite the flame, a gas mixture of CH_4 and air is introduced at an axial velocity of 1.11 m/s and a temperature of 400 K from the secondary stream as a pilot flame with equivalence ratio of unity. CH_4 in the secondary stream

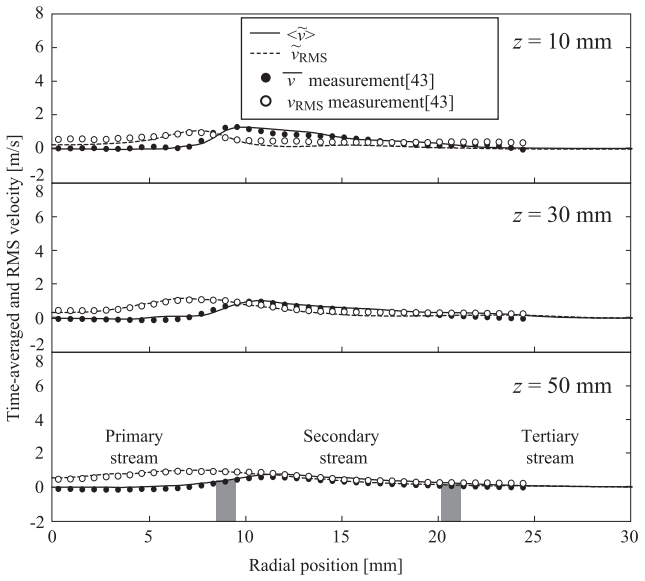

Fig. 4c. Comparisons of radial distributions of time-averaged and RMS velocities in circumferential direction at three downstream locations between measurement and LES for non-reacting flows. (See above-mentioned references for further information.)

is immediately consumed by a reaction model, in which two-step global mechanisms [44] are considered, near the burner outlet and which does not affect the reaction in the downstream region. In the outer tertiary stream, a laminar air flow is introduced at an axial velocity of 0.37 m/s and a temperature of 300 K. The whole computational domain is divided into about 7 million hexahedral grids, and the minimum mesh size is about 300 μm near the region close to burner outlet.

2.4. Coal properties

The coal sample used in this study is Cerrejon, whose properties are listed in Table 2. The size distribution of the coal used in the experiment [43] indicates that around 50% of particles have diameters below 75 μm, another 40% are between 75 and 500 μm, and the remainder above 500 μm in size. In present LES, on the other hand, the size distribution of the coal must be compatible with the requirement associated with the grid size from the point of view of numerical accuracy (the grid spacing needs to be roughly 10 times larger than the particle size to get enough accuracy by using the PSI-Cell method [45]). The size distribution is assumed to be represented by aRosin–Rammler distribution, in which the specific diameter and spread parameter are given as 40 μm and 2, respectively. To reduce the computational cost, representative coal particles, i.e., parcels, are tracked in time instead of all coal

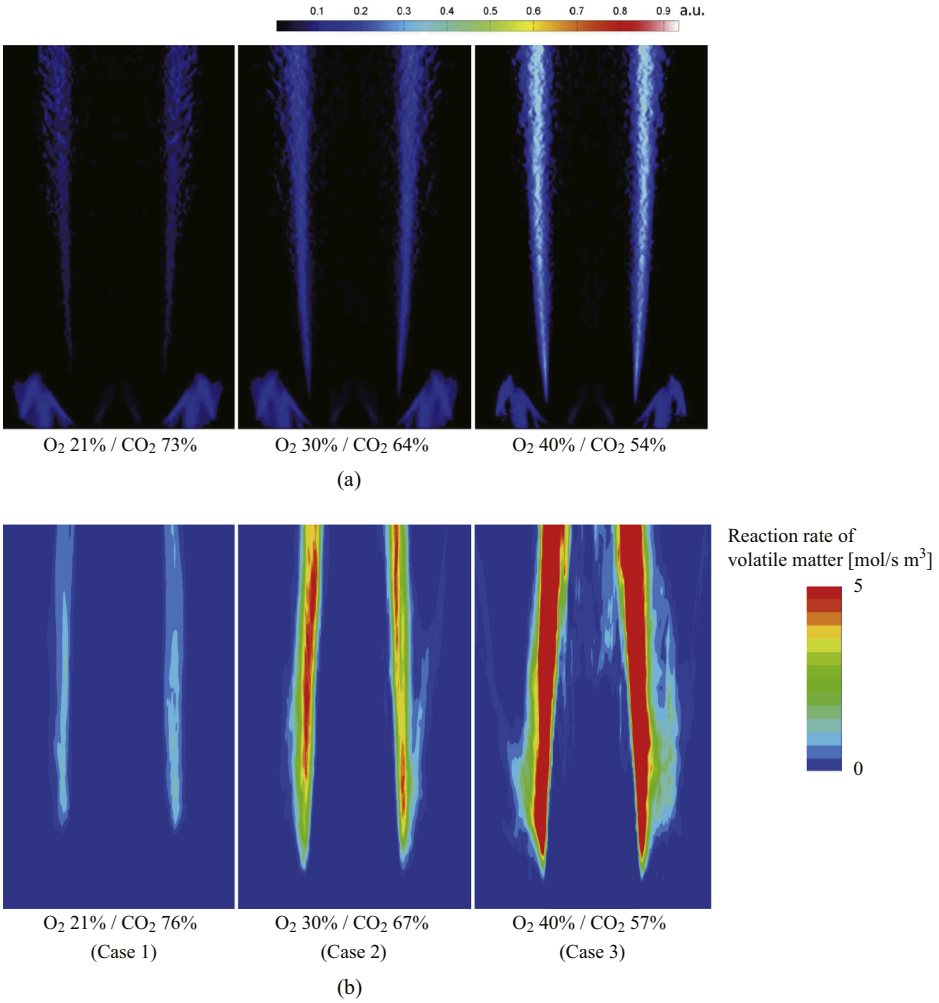

Fig. 5. Comparison between (a) Abel inverted OH* images [43] and (b) reaction rate of volatile matter by present LES at equivalence ratio of 1.73.

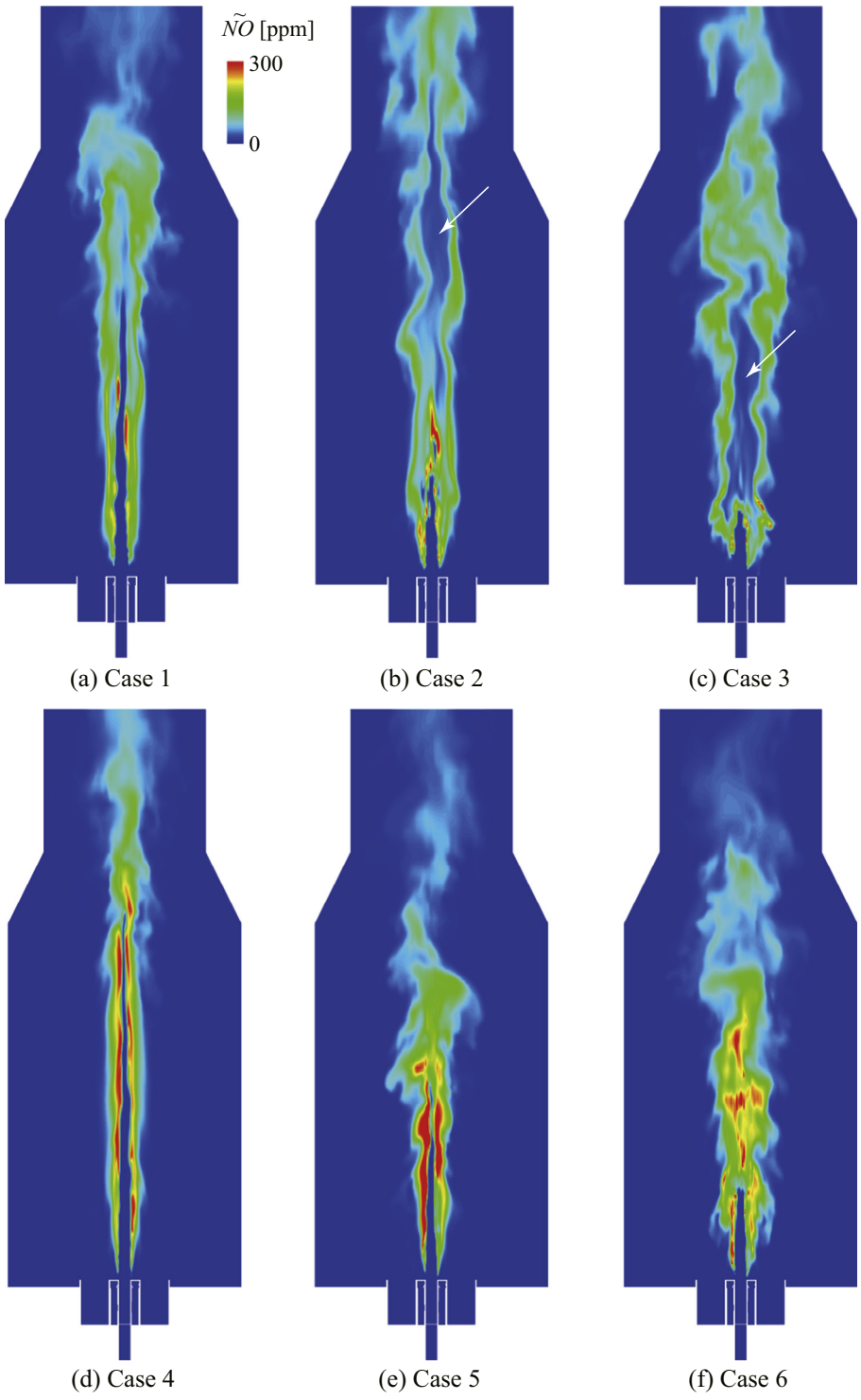

Fig. 6. Instantaneous distributions of NO concentration $\widetilde{NO}$ on the x–z plane at $y = 0$ mm.

particles. About 0.3 million parcels exist in the computational domain during the computation.

3. Results and discussion

3.1. General features of coal jet flame and comparison with experiment

Fig. 2 shows the instantaneous distributions of Favre-filtered quantities, (a) axial velocity $\tilde{w}$, (b) gas temperature $\tilde{T}$, and (c) mole fractions of volatile matter $\tilde{X}_{VM}$, (d) O_2 $\tilde{X}_{O_2}$, and RMS values of (e) axial velocity $\tilde{w}_{RMS}$, and (f) gas temperature $\tilde{T}_{RMS}$, on the x–z plane for Case 1. Here, the tilde denotes the Favre filtered value for any quantity, ϕ. RMS fluctuation is defined by $\tilde{\phi}_{RMS} = \sqrt{\langle \tilde{\phi}'^2 \rangle}$, where $\tilde{\phi} = \langle \tilde{\phi} \rangle + \tilde{\phi}'$ and $\langle\ \rangle$ denotes time-averaged values. The time-averaged and RMS values are evaluated by using the data from $t = 1.0$–1.2 s which corresponds 20,000 calculation steps. It is observed that the coal particles are ignited by the pilot flame of secondary stream, and the coal flame is lifted up to a point where $\tilde{w}_{RMS}$ and $\tilde{T}_{RMS}$ show high values. Part of the released volatile

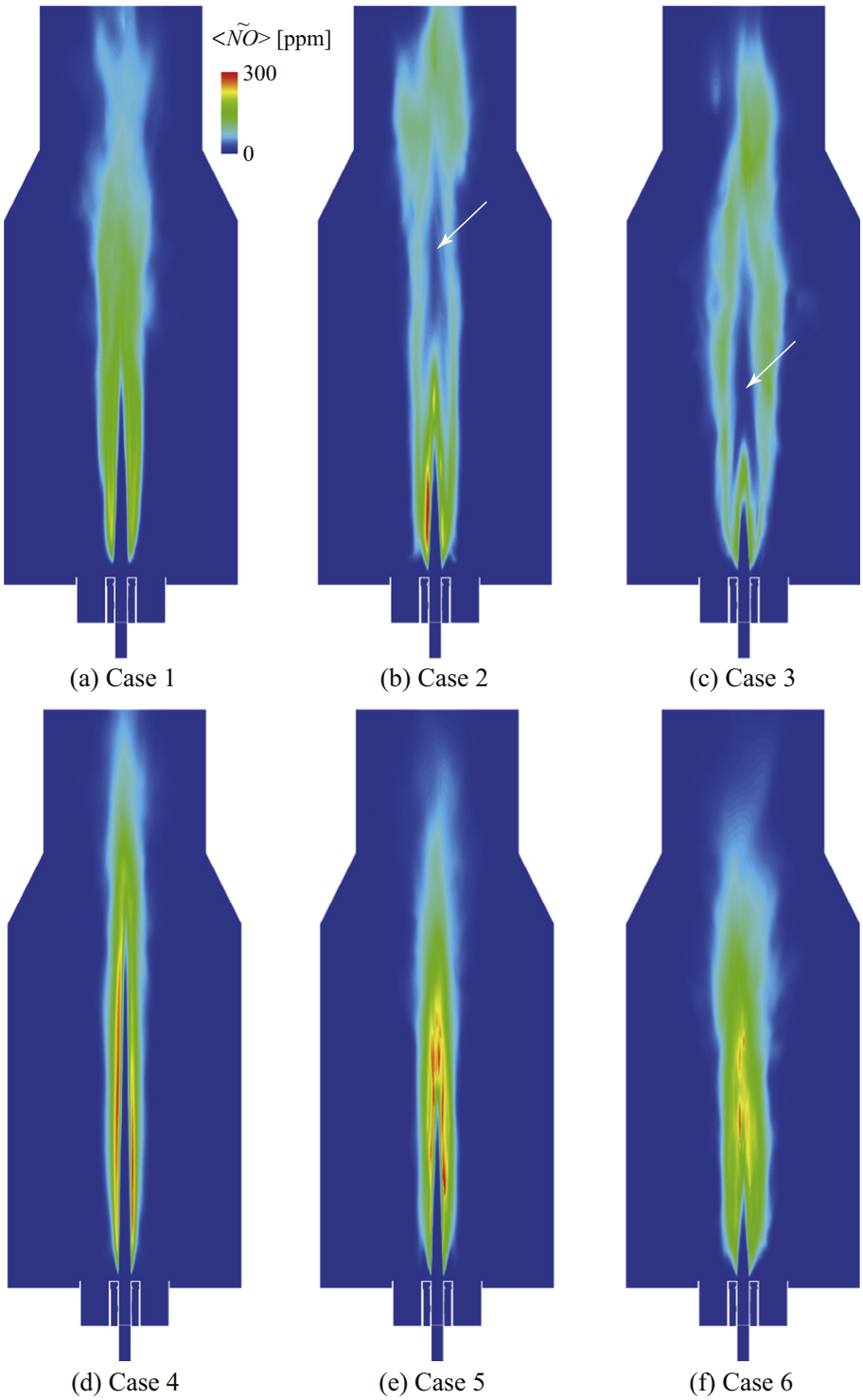

Fig. 7. Time-averaged distributions of NO concentration $\langle \tilde{NO} \rangle$ on the x–z plane at $y = 0$ mm.

matter is consumed by O_2 oxidation near the burner outlet, whereas most of it remains unburned in the downstream region due to the lack of O_2, because the equivalence ratio for Case 1 is larger than unity.

Fig. 3 shows the instantaneous distributions of coal particles colored by (a) particle temperature T_p, and mass fractions of (b) volatile matter $Y_{p,VM}$, and (c) fixed carbon $Y_{p,FC}$, in the particles behind the x–z plane at $y = 0$ mm for Case 1. It is found that the temperature of the particles facing the secondary streams rapidly increases and that $Y_{p,VM}$ and $Y_{p,FC}$ in the particles decreases and increases, respectively. This means that the oxidizing reaction of fixed carbon hardly occurs and the rapid increase in T is attributed mainly to the combustion of volatile matter.

Figs. 4a–4c shows the comparisons of time-averaged and RMS of velocity between present and experimental results [43] in the non-reacting condition at $z = 10$, 30 and 50 mm along the axial

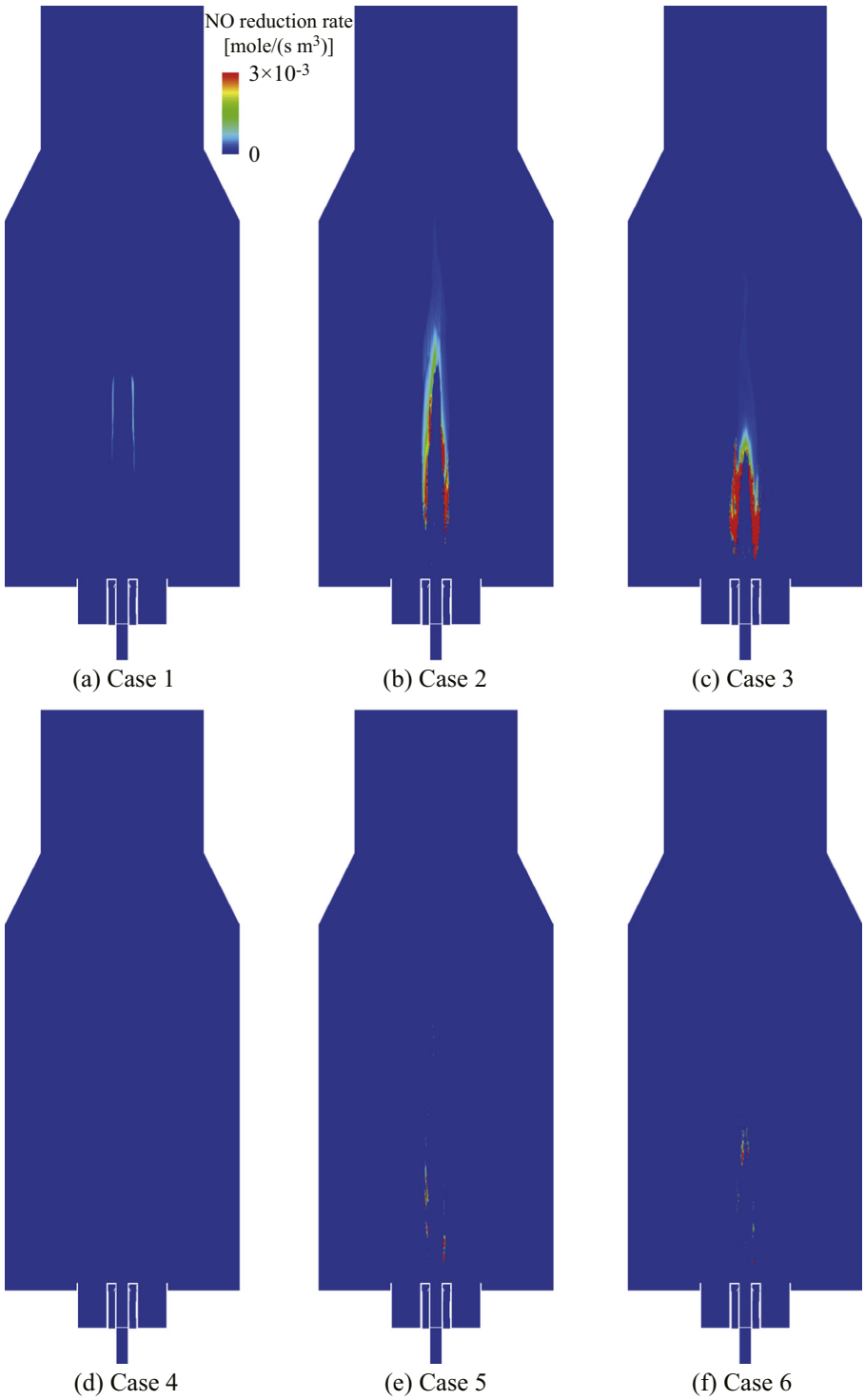

Fig. 8. Time-averaged distributions of NO reduction rate on the x–z plane at $y = 0$ mm.

direction. For experiment, RMS velocity in axial direction is defined by $w_{RMS} = \sqrt{\overline{w'^2}}$, where $w = \overline{w} + w'$ and overline denotes time-averaged value. This definition is the same as for other directions. As seen in the figures, it is confirmed that the behaviors of the experimental results [43] are quantitatively well captured by present LES.

Fig. 5 shows the instantaneous distributions of (a) Abel inverted OH^* chemiluminescence obtained by the experiment [43] and (b) reaction rate of volatile matter predicted by present LES on the x–z plane at $y = 0$ mm for the cases with equivalence ratio of 1.73. The OH^* radical is considered to be generated in the region where the volatile matter is consumed and the heat of combustion is released remarkably. The experiment shows that the peak value of the intensity of OH^* radical rises with increasing O_2 concentration. This is attributed to the fact that the reaction rate of volatile matter is promoted by higher O_2 concentrations and suppressed by the higher specific heat capacity of CO_2. This behavior is also captured by present LES. However, the LES result slightly overestimates the inward distribution of the reaction rate region further downstream, as compared to the experiment. This may be a result

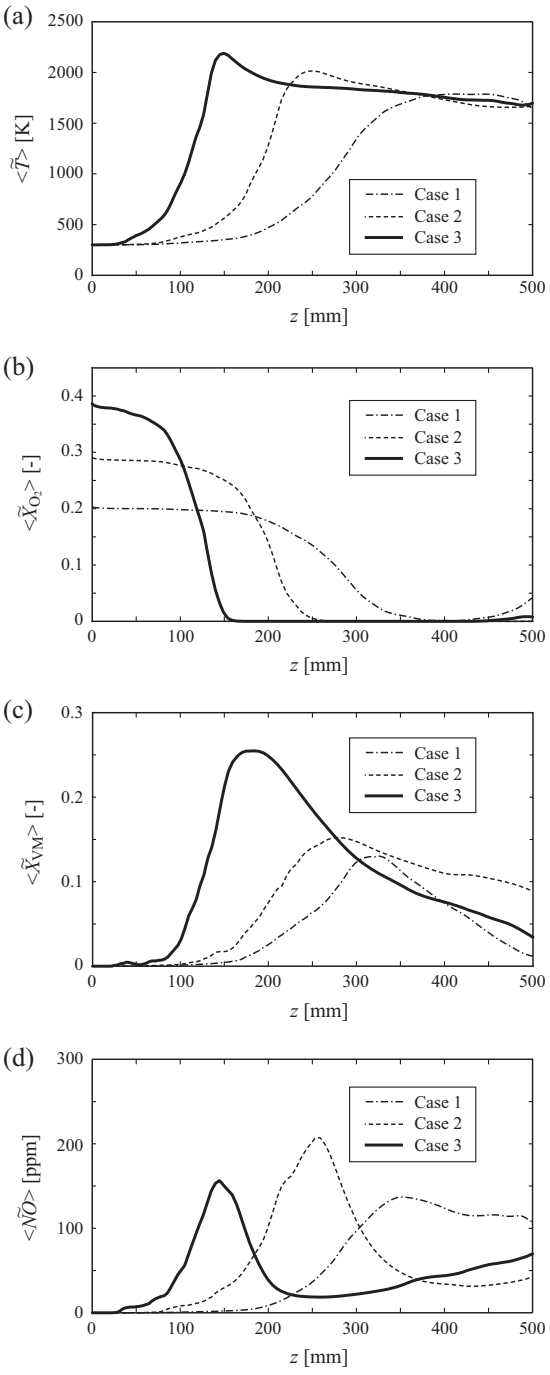

Fig. 9. Time-averaged axial distributions of (a) gas temperature $\langle\tilde{T}\rangle$, and mole fractions of (b) O_2 $\langle\tilde{X}_{O_2}\rangle$, (c) volatile matter $\langle\tilde{X}_{VM}\rangle$ and (d) NO concentration $\langle\tilde{NO}\rangle$ at equivalence ratio of 1.73.

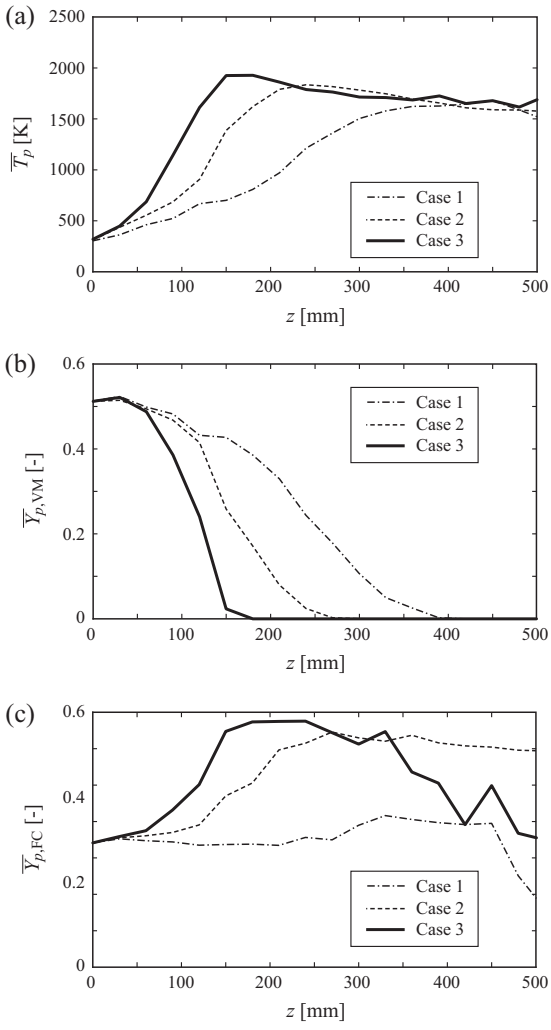

Fig. 10. Time-averaged axial distributions of (a) particle temperature $\overline{T}_p$, and mass fractions of (b) volatile matter $\overline{Y}_{p,VM}$ and (c) fixed carbon $\overline{Y}_{p,FC}$ in coal particles at equivalence ratio of 1.73.

of a higher estimate of reaction rates and corresponding temperatures by the devolatilization model and two-step global reaction model for combustion of volatile matter used in present study. A contributing factor may also be the smaller diameter distribution of the pulverized coal used in the computations compared to the experimental values.

3.2. Effects of the O_2 concentration on NO formation

The instantaneous and time-averaged distributions of NO concentration on the x–z plane at $y = 0$ mm for Cases 1–6 are shown in Figs. 6 and 7. For all cases, NO formation starts to increase from where $\tilde{T}$ starts to increase (see Fig. 2(b)). I particular, for Cases 2 and 3 with equivalence ratio of 1.73, there appear low NO concentration pockets (indicated by white arrows) which shift upstream with increasing O_2 concentration. On the other hand, the NO concentration pockets cannot be observed for the cases with equivalence ratio of 0.64 (Cases 4–6) for both instantaneous and time-averaged distributions. The generation of the low NO concentration pockets for the cases with high equivalence ratio are attributed to the rapid decrease in O_2 in the downstream region.

The time-averaged distributions of the reduction rate of NO on the x–z plane at $y = 0$ mm for Cases 1–6 are shown in Fig. 8. Regardless the equivalence ratio, the reduction is not significant for low O_2 concentrations. For, Cases 2 and 3 with equivalence ratio of 1.73, there appears to be a high NO reduction rate just upstream the NO concentration pockets seen in Fig. 7. These high NO reduction rate regions appear due to the reburn process and Levy's model described in Section 2.2. However, in Cases 5 and 6 with equivalence ratio of 0.64, the region with high NO reduction rate is small.

Fig. 9 shows the time-averaged axial distributions of (a) gas temperature $\langle\tilde{T}\rangle$, mole fractions of (b) O_2 $\langle\tilde{X}_{O_2}\rangle$, (c) volatile matter $\langle\tilde{X}_{VM}\rangle$, and (d) NO concentration $\langle\tilde{NO}\rangle$, for the cases of equivalence ratio 1.73. The distribution of $\langle\tilde{T}\rangle$ confirms that the location of

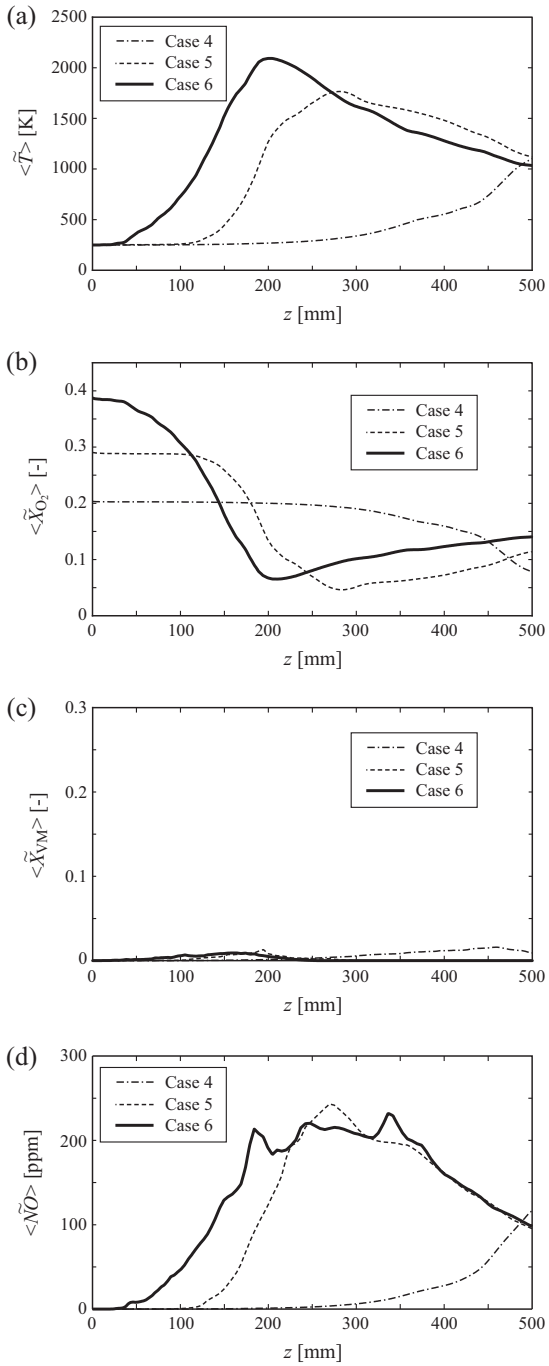

Fig. 11. Time-averaged axial distributions of (a) gas temperature $\langle\tilde{T}\rangle$, and mole fractions of (b) O_2 $\langle\tilde{X}_{O_2}\rangle$, (c) volatile matter $\langle\tilde{X}_{VM}\rangle$ and (d) NO concentration $\langle\tilde{NO}\rangle$ at equivalence ratio of 0.69.

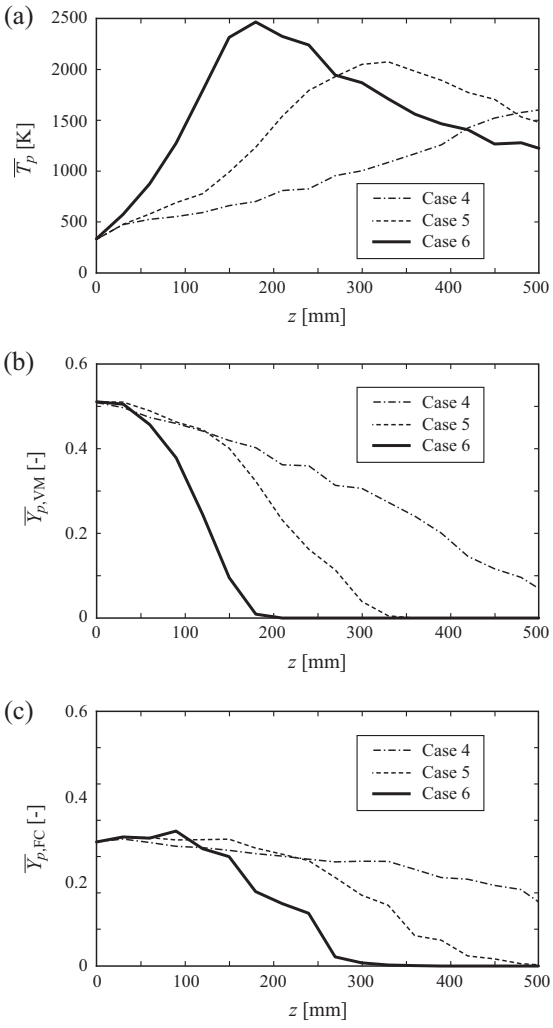

Fig. 12. Time-averaged axial distributions of (a) particle temperature $\overline{T}_p$, and mass fractions of (b) volatile matter $\overline{Y}_{p,VM}$ and (c) fixed carbon $\overline{Y}_{p,FC}$ in coal particles at equivalence ratio of 0.69.

ignition of the coal particles shifts upstream with increasing O_2 concentration, which increases reaction rate. For all three cases, $\langle\tilde{X}_{VM}\rangle$ increases as $\langle\tilde{T}\rangle$ increases, and the location indicating peak value of $\langle\tilde{X}_{VM}\rangle$ is consistent with the location indicating the peak value of $\langle\tilde{T}\rangle$. The peak value in $\langle\tilde{X}_{VM}\rangle$ increases with increasing O_2 concentrations, as the increase in reaction enhances devolatilization. And this increase in the peak value is also observed by an increase of coal feeding rate with increasing the O_2 concentration and decreasing the CO_2 concentration (see Table 1). Focusing on the NO formation behavior, the locations where $\langle\tilde{NO}\rangle$ rapidly increases and reaches a few hundred ppm correspond to the locations indicating the peak values of $\langle\tilde{T}\rangle$. This is followed by rapid decreases in $\langle\tilde{NO}\rangle$, especially for Cases 2 and 3. The decrease in $\langle\tilde{NO}\rangle$ after its peak is caused by the reducing atmosphere and associated with the low NO concentration pockets seen in Figs. 6 and 7. The peak value in the $\langle\tilde{NO}\rangle$ increases with increasing O_2 concentration from Cases 1 to 2, but decreases from Cases 2 to 3 despite of the higher $\langle\tilde{T}\rangle$ and $\langle\tilde{X}_{VM}\rangle$. This is attributed to the strong reducing atmosphere in the downstream region of the peak value in $\langle\tilde{NO}\rangle$, which suppresses the NO formation.

Fig. 10 shows the time-averaged axial distributions of (a) particle temperature $\overline{T}_p$, mass fractions of (b) volatile matter $\overline{Y}_{p,VM}$, and (c) fixed carbon $\overline{Y}_{p,FC}$, for the cases of equivalence ratio of 1.73. It is found that the behavior of $\overline{T}_p$ is consistent with that of $\langle\tilde{T}\rangle$ in Fig. 9, that is, the locations where the peak values of $\overline{T}_p$ appear to shift upstream with increasing O_2 concentration. The rapid decreases of $\overline{Y}_{p,VM}$ are also consistent with the rapid increases of $\langle\tilde{X}_{VM}\rangle$ in Fig. 9. The interesting behavior is observed in $\overline{Y}_{p,FC}$: the value for Cases 2 and 3 increases as $\overline{T}_p$ increases, because the devolatilization rate is higher than the reaction rate of fixed carbon. On the other hand, $\overline{Y}_{p,FC}$ for Case 1 remains the same up to $z = 450$ mm. This means that the reaction rate of the fixed carbon is comparable with the devolatilization rate of the volatile matter. This is consistent with the fact that devolatilization rates for Case 1 are lower than those for Cases 2 and 3 due to low $\overline{T}_p$, whereas the oxidation reaction of fixed carbon proceeds because of the remaining O_2 in the downstream region. One of the reasons why the apparent NO

reduction behavior does not appear for Case 1 in the distribution of $\langle \tilde{NO} \rangle$ (see Fig. 9) is considered that NO is also formed by the oxidation reaction of fixed carbon, namely char NO.

Fig. 11 shows time-averaged axial distributions of (a) gas temperature $\langle \tilde{T} \rangle$, mole fractions of (b) O_2 $\langle \tilde{X}_{O_2} \rangle$, (c) volatile matter $\langle \tilde{X}_{VM} \rangle$, and (d) NO concentration $\langle NO \rangle$, for the cases of equivalence ratio of 0.64. The comparisons with the cases of equivalence ratio of 1.73 (Cases 1–3) show that $\langle \tilde{X}_{VM} \rangle$ for Cases 4–6 are much lower than those for Cases 1–3 because of the lean conditions such that excess O_2 remains in the downstream region as seen in $\langle \tilde{X}_{O_2} \rangle$. Focusing on the NO formation behavior, $\langle \tilde{NO} \rangle$ rapidly increases and reaches a few hundred ppm, similarly to Cases 1–3. However, the NO reduction behavior cannot be clearly observed for Cases 5 and 6 because sufficient O_2 remains in the downstream region.

Fig. 12 shows the time-averaged axial distributions of (a) particle temperature $\overline{T}_p$, mass fractions of (b) volatile matter $\overline{Y}_{p,VM}$, and (c) fixed carbon of particles $\overline{Y}_{p,FC}$, for the cases of equivalence ratio of 0.64. The comparisons with cases with equivalence ratio 1.73 (Cases 1–3) show that the peak values of $\overline{T}_p$ are higher than those for Cases 1–3, and the locations where the peak values appear tend to shift downstream compared to those for Cases 1–3. Consequently, the locations where the peak values of $\overline{Y}_{p,VM}$ appear tend to shift downstream as well. The trends in $\overline{Y}_{p,FC}$ for Cases 4–6 are quite different from those for Cases 1–3, namely $\overline{Y}_{p,FC}$ never increases during devolatilization. This suggests that oxidation reaction of fixed carbon occurs due to the abundant O_2 and it is considered that char NO is also formed during the oxidation larger than that for Cases 1–3. Thus, it appears that the difference in NO formation behavior between the cases of equivalence ratio of 1.73 (Cases 1–3) and the cases of equivalence ratio of 0.64 (Cases 4–6) is caused by the complex balance of NO reduction and NO formation by combustion of volatile matter and fixed carbon in the reducing and oxidizing atmosphere formed in the coal flames.

4. Conclusions

In this study, the effects of the O_2 concentration and equivalence ratio on the formation process of NO in a laboratory-scale open-type pulverized coal flame generated by a triple stream burner were investigated by means of LES under oxy-firing conditions in which O_2/CO_2 mixture is used as oxidizer. The main results obtained in this study can be summarized as follows.

- Regardless of the equivalence ratio, as the O_2 concentration increases from 21% to 40%, O_2 consumption becomes marked because gas temperature rises and oxidation reaction is enhanced by the higher concentration of O_2.
- NO is formed rapidly due to the oxidation reaction of N_2 from volatile matter of coal and its axial profile reaches a few hundred ppm further downstream. After rapid formation, in the case of equivalence ratio larger than unity, NO decreases because the reducing atmosphere becomes dominant due to the lack of O_2. The trend tends to be remarkable as the O_2 concentration increases from 21% to 40%. In the case of equivalence ratio less than unity, however, NO does not decrease, apparently because an oxidizing atmosphere prevails.
- The present study presents for the first time LES predictions of NO production and reduction in oxy-fuel conditions, partially validated by experimental findings, which verifies the usefulness of the LES to predict the characteristics of pulverized coal flames.

Acknowledgments

The authors are grateful to Drs. Huirai Zhang and Kotaro Hori of Numerical Flow Designing CO., Ltd. for many useful discussions. The authors also would like to thank Mr. Takeshi Iwata for conducting numerical simulations. This research was partially supported by "Strategic Programs for Innovative Research (SPIRE) – Field No. 4: Industrial Innovations" from MEXT (Ministry of Education, Culture, Sports, Science, and Technology) using computational resources of the HPCI system provided by RIKEN Advanced Institute for Computational Science through the HPCI System Research Project (Project ID: hp120294, hp130018). See also (http://www.fluid.me.kyoto-u.ac.jp/members/kurose/hpci.html). Experiments at Cambridge were supported by EPSRC, within the Oxycap Oxyfuels Grant EP/G062153/1.

References

[1] IEA Natural Gas Prospects to 2010. International Energy Agency; 1986.
[2] Singh D, Croiset E, Douglas PL, Douglas MA. Techno-economic study of CO_2 capture from an existing coal-fired power plant: MEA scrubbing vs. O_2/CO_2 recycle combustion. Energy Convers Manage 2003;44:3073–91.
[3] Buhre BJP, Elliott LK, Sheng CD, Gupta RP, Wall TF. Oxy-fuel combustion technology for coal-fired power generation. Prog Energy Combust Sci 2005;31:283–307.
[4] Wall TF. Combustion processes for carbon capture. Proc Combust Inst 2007;31:31–47.
[5] Edge P, Gharebaghi M, Irons R, Porter R, Porter RTJ, Pourkashanian M, Smith D, Stephenson P, Williams A. Combustion modelling opportunities and challenges for oxy-coal carbon capture technology. Chem Eng Res Des 2011;89:1470–93.
[6] Chen L, Yong SZ, Ghoniem AF. Oxy-fuel combustion of pulverized coal: characterization, fundamentals, stabilization and CFD modeling. Prog Energy Combust Sci 2012;38:156–214.
[7] Kurose R, Makino H, Suzuki A. Numerical analysis of pulverized coal combustion characteristics using advanced low-NO_x burner. Fuel 2004;83:693–703.
[8] Kurose R, Ikeda M, Makino H. Combustion characteristics of high ash coal in a pulverized coal combustion. Fuel 2001;80:1447–55.
[9] Kurose R, Tsuji H, Makino H. Effects of moisture in coal on pulverized coal combustion characteristics. Fuel 2001;80:1457–65.
[10] Kurose R, Watanabe H, Makino H. Numerical simulations of pulverized coal combustion. KONA Powder Part J 2009;27:144–56.
[11] Hashimoto N, Kurose R, Tsuji H, Shirai H. A numerical analysis of pulverized coal combustion in a multiburner furnace. Energy Fuels 2007;21:1950–8.
[12] Hashimoto N, Kurose R, Hwang SM, Tsuji H, Shirai H. A numerical simulation of pulverized coal combustion employing a tabulated-devolatilization-process model (TDP model). Combust Flame 2012;159:353–66.
[13] Hashimoto N, Kurose R, Shirai H. Numerical simulation of pulverized coal jet flame using the TDP model. Fuel 2012;97:277–87.
[14] Al-Abbas AH, Naser J, Hussein EK. Numerical simulation of brown coal combustion in a 550 MW tangentially-fired furnace under different operating conditions. Fuel 2013;107:688–98.
[15] Hashimoto N, Shirai H. Numerical simulation of sub-bituminous coal and bituminous coal mixed combustion employing tabulated-devolatilization-process model. Energy 2014;71:399–413.
[16] Kurose R, Makino H. Large eddy simulation of a solid–fuel jet flame. Combust Flame 2003;135:1–16.
[17] Watanabe H, Tanno K, Baba Y, Kurose R, Komori S. Large-eddy simulation of coal combustion in a pulverized coal combustion furnace with a complex burner. In: Hanjalic' K, Nagano Y, Jakirlic S, editors. Turbulence, heat and mass transfer, vol. 6; 2009. p. 1027–30.
[18] Yamamoto K, Murota T, Okazaki T, Taniguchi M. Large eddy simulation of a pulverized coal jet flame ignited by a preheated gas flow. Proc Combust Inst 2011;33:1771–8.
[19] Franchetti BM, Marincola FC, Navarro-Martinez S, Kempf AM. Large eddy simulation of a pulverized coal jet flame. Proc Combust Inst 2013;34:2419–26.
[20] Stein OT, Olenik G, Kronenburg A, Marincola FC, Franchetti BM, Kempf AM, Ghiani M, Vascellari M, Hasse C. Towards comprehensive coal combustion modeling for LES. Flow Turbul Combust 2013;90:859–84.
[21] Abani N, Ghoniem AF. Large eddy simulations of coal gasification in an entrained flow gasifier. Fuel 2013;104:664–80.
[22] Watanabe J, Yamamoto K. Flamelet model for pulverized coal combustion. Proc Combust Inst 2014. http://dx.doi.org/10.1016/j.proci.2014.07.065.
[23] Rabacal M, Franchetti BM, Marincola FC, Proch F, Costa M, Hasse C, Kempf AM. Large eddy simulation of coal combustion in a large-scale laboratory furnace. Proc Combust Inst 2014. http://dx.doi.org/10.1016/j.proci.2014.06.023.
[24] Olenik G, Stein OT, Kronenburg A. LES of swirl-stabilised pulverised coal combustion in IFRF furnace No. 1. Proc Combust Inst 2014. http://dx.doi.org/10.1016/j.proci.2014.06.149.
[25] Edge P, Gubba SR, Ma L, Porter R, Pourkashanian M, Williams A. LES modelling of air and oxy-fuel pulverised coal combustion – impact on flame properties. Proc Combust Inst 2011;33:2709–16.
[26] Nikolopoulos N, Nikolopoulos A, Karampinis E, Grammelis P, Kakaras E. Numerical investigation of the oxy-fuel combustion in large scale boilers adopting the ECO-Scrub technology. Fuel 2011;90:198–214.

[27] Taniguchi M, Yamamoto K, Okazaki T, Rehfeldt S, Kuhr C. Application of lean flammability limit study and large eddy simulation to burner development for an oxy-fuel combustion system. Int J Greenhouse Gas Control 2011;5:S111–9.
[28] Jovanovic R, Rasuo B, Stefanovic P, Cvetinovic D, Swiatkowski B. Numerical investigation of pulverized coal jet flame characteristics under different oxy-fuel conditions. Int J Heat Mass Transfer 2013;58:654–62.
[29] Pedel J, Thornock JN, Smith ST, Smith PJ. Large eddy simulation of polydisperse particles in turbulent coaxial jets using the direct quadrature method of moments. Int J Heat Mass Transfer 2014;63:23–38.
[30] Chen L, Ghoniem AF. Simulation of oxy-coal combustion in a 100 kWth test facility using RANS and LES: a validation study. Energy Fuels 2012;26:4783–98.
[31] Niksa S. Predicting the devolatilization behavior of any coal from its ultimate analysis. Combust Flame 1995;100:384–94.
[32] Field MA. Rate of combustion of size-graded fractions of char from a low-rank coal between 1200 K and 2000 K. Combust Flame 1969;13:237–51.
[33] Kim J, Moin P. Application of a fractional-step method to incompressible Navier–Stokes equations. J Comput Phys 1985;59:308–23.
[34] Fenimore CP. Formation of nitric oxide in premixed hydrocarbon flames. In: Proceedings of 13th symposium (international) on combustion, vol. 13; 1971. p. 373–80.
[35] Bedat B, Egolfopoulos FN, Poinsot T. Direct numerical simulation of heat release and NOx formation in turbulent nonpremixed flames. Combust Flame 1999;119:69–83.
[36] Mitchell JW, Tarbell JM. A kinetic model of nitric oxide formation during pulverized coal combustion. AlCHE J 1982;28-2:302–11.
[37] De Soete GG. Overall reaction rates of NO and N_2 formation from fuel nitrogen. In: Proceedings of 15th symposium (international) on combustion; 1975. p. 1093–102.
[38] De Soete GG. Heterogeneous N_2O and NO formation from bound nitrogen atoms during coal char combustion. In: Proceedings of 23rd symposium (international) on combustion; 1990. p. 1257–64.
[39] Levy JM, Chan LK, Sarofim AF, Beer JM. NO/char reactions at pulverized coal flame conditions. In: Proceedings of 18th symposium (international) on combustion; 1981. p. 111–20.
[40] DesJardin PE, Frankel SH. Large eddy simulation of a nonpremixed reaction jet: application and assessment of subgrid-scale combustion models. Phys Fluids 1998;10:2298–314.
[41] Kurose R, Makino H, Michioka T, Komori S. Large eddy simulation of a nonpremixed turbulent reacting mixing layer: effects of heat release and spanwise fluid shear. Combust Flame 2001;127:2159–65.
[42] Balusamy S, Schmidt A, Hochgreb S. Flow field measurements of pulverized coal combustion using optical diagnostic techniques. Exp Fluids 2013;54:1534–48.
[43] Balusamy S, Hochgreb S. Flow field measurements of pulverized coal combustion in oxyfuel condition using laser diagnostic techniques. In: Proceedings of the European combustion meeting; 2013. p. P5-15.
[44] Westbrook CK, Dryer FL. Simplified reaction mechanisms for the oxidation of hydrocarbon fuels in flames. Combust Sci Technol 1981;27:31–43.
[45] Luo K, Pitsch H, Pai MG, Desjardins O. Direct numerical simulations and analysis of three-dimensional n-heptane spray flames in a model swirl combustor. Proc Combust Inst 2011;33:2143–52.